Nanoscale magnetism probed by nuclear resonant scattering of synchrotron radiation

R. Röhlsberger, J. Bansmann, V. Senz, K. L. Jonas, A. Bettac, and K. H. Meiwes-Broer
Universität Rostock, Universitätsplatz 3, 18055 Rostock, Germany

O. Leupold
European Synchrotron Radiation Facility, Boîte Postale 220, 38043 Grenoble Cedex, France
(Received 27 October 2002; published 26 June 2003; publisher error corrected 30 June 2003)

Time-resolved nuclear resonant scattering of synchrotron radiation is applied to determine the spin structure of magnetic nanostructures on surfaces. From the temporal beat pattern the magnitude and the direction of magnetic hyperfine fields in the sample can be determined. We describe an algorithm to extract the magnetic structure function from a series of such measurements at different sample orientations. This reconstruction technique is applied to study the remanent spin structure of relaxed Fe islands on the surface of a W(110) single crystal. Unexpectedly, we find two orthogonal magnetic sublattices oriented along the in-plane [001] and $[1\bar{1}0]$ directions in a proportion of 4:1. This spin structure appears to be independent of capping layers that consist of Ag or C. A completely different spin structure is found for a different shape distribution of the islands. These results are discussed in terms of magnetic anisotropies that are present in this system. Moreover, the results demonstrate that the outstanding brilliance of present-day synchrotron-radiation sources allows one to determine the magnetic spin structure of magnetic clusters and nanoparticles on surfaces with sensitivities reaching into the monolayer regime.

DOI: 10.1103/PhysRevB.67.245412 PACS number(s): 75.25.+z, 75.75.+a, 36.40.Cg, 76.80.+y

I. INTRODUCTION

Magnetic thin films and nanostructures display a richness of magnetic properties that do not have a bulk counterpart.[1] These phenomena challenge the understanding of magnetism on the atomic scale and its origin. In addition, they are of outmost technological relevance due to applications in magnetic data storage and in the growing field of magnetoelectronics.[2,3] Parallel to the decreasing size of magnetic microstructures, there is a growing need for efficient methods to characterize magnetic properties on the atomic level. In the last decade, a number of techniques have been developed for direct imaging of magnetic nanostructures.[4] One class of methods is based on the detection of secondary electrons after absorption of photons or electrons. The image contrast is achieved due to magnetic dichroism in photoabsorption as in the case of photoemission electron microscopy[5] or due to detection of spin-polarized electrons as in case of scanning electron microscopy with polarization analysis.[6] Another class of methods relies on scanning probe techniques such as magnetic force microscopy[7] or spin-polarized scanning tunneling microscopy.[8] While the former methods yield lateral resolutions in the range of 10–100 nm, the latter method allows one to image magnetic structures with atomic resolution.[9] However, due to the shallow escape depth of electrons from solids and the limited probing depth of scanning probe methods, these methods are often too surface sensitive. A larger probing depth can be achieved via scattering methods such as polarized neutron scattering[10] or magnetic x-ray scattering.[11] In these cases, information about the magnetic structure can be obtained via diffraction experiments. The magnetic structure is then reconstructed from data recorded in reciprocal space, therefore this class of methods can be considered complementary to real-space imaging methods. While polarized neutron scattering is used to investigate bulk magnetic systems since long, experiments on small sample volumes such as ultrathin films often suffer from the low brilliance of neutron sources. On the other hand, the outstanding brilliance of x-ray synchrotron radiation has opened unique experimental possibilities to study magnetic properties of surfaces and nanoscale structures in recent years.[11] This is particularly true for the technique of nuclear resonant scattering of synchrotron radiation.[12] The method is the time-based analog of classical Mössbauer spectroscopy with synchrotron radiation as a source. Due to the pulsed time structure hyperfine spectroscopy is performed on a time scale rather than on an energy scale. The simultaneous excitation of the hyperfine-split nuclear energy levels by a radiation pulse leads to quantum beats in the temporal evolution of the nuclear decay. The analysis of this beat pattern allows a precise determination of the magnitude and the orientation of magnetic fields in the sample. While nuclear resonant absorption as used in conventional Mössbauer spectroscopy is an *incoherent* process that reflects the local environment of individual nuclei, *coherent* scattering processes are also sensitive to the spatial arrangement of the nuclei, giving rise to diffraction or other interference effects. However, the brilliance of radioactive sources is too low for an effective application of coherent scattering from thin films, so that only a few experiments have been reported since the discovery of the Mössbauer effect.[13–17] This situation changed drastically with the availability of high-brilliance synchrotron-radiation sources. Since then, a number of thin-film and multilayer systems have been studied,[18–22] with sensitivities in the monolayer regime.[23,24]

Fe on W(110) is an ideal model system to study the interplay of various magnetic anisotropies in ultrathin films.[25] This system exhibits a positive surface energy that allows for the formation of stable films in contrast to metastable configurations such as Fe/Cu. The pseudomorphic Fe monolayer

on W(110) was the first system in which two-dimensional ferromagnetic order was observed, induced by a large surface anisotropy.[26] The magnetic order in thin films of Fe on W(110) was then extensively investigated.[27–34] Particularly interesting are self-organized magnetic structures that form in special growth conditions. For example, at coverages in the submonolayer range one observes the formation of separated islands[31] that order with a perpendicular anisotropy at low temperatures.[24] The double-layer patches that form at coverages of about 1.5 ML exhibit perpendicular anisotropy and antiferromagnetic coupling.[32–34] For continuous Fe films one observes a reorientation of the in-plane easy axis at thickness of about 50 ML.[25] If thinner films are annealed at sufficiently high temperatures, they form separated three-dimensional islands[35] with the lattice constant of bcc Fe. So far, however, only a few experiments are reported about the magnetic order of these islands.[36–38]

In this paper, we employ the method of nuclear resonant scattering of synchrotron radiation at the 14.4-keV resonance of ^{57}Fe to study the magnetism of such self-organized nanoscale Fe islands. The paper is organized as follows. In the first section, we outline a compact formulation of polarization-dependent x-ray scattering in grazing-incidence geometry. The formalism is applicable to many types of resonant scattering problems. In the following section, we discuss the scattering amplitude for coherent nuclear scattering that determines the optical properties of thin films. In the case of ultrathin films, the scattering can be treated in the kinematical limit that allows for a simple analytical treatment of the scattering problem. It is shown how the quantum beat pattern of the time response serves as a fingerprint for the magnetic structure of the sample. However, a unique reconstruction is only possible if measurements are performed for a number of different orientations of the sample. We use an algorithm to extract the magnetic structure function from a set of measured time spectra. In the experimental section, this method is applied to determine the magnetic structure of self-organized Fe islands on W(110) with different shapes and various capping layers. In general, this technique is applicable to low-dimensional systems such as ultrathin films and nanoparticles deposited in thin films and on surfaces, for example, as will be discussed in the concluding section.

II. BASIC PRINCIPLES

A. Grazing-incidence magnetic x-ray scattering

The presence of a finite sample magnetization often renders the scattering of x rays strongly polarization sensitive. This effect is particularly pronounced if the photon energy is close to an inner-shell or a nuclear resonance. In this case, the dynamical theory of x-ray scattering has to take into account the polarization dependence of the scattering process, as explained in the following.

To describe the propagation of electromagnetic waves in homogeneous materials, a self-consistent solution for the electromagnetic wave field under consideration of all multiple-scattering processes has to be found. This is subject of the dynamical theory of x-ray scattering, see, e.g., Ref. 39. Formally, in any of the formulations developed so far one

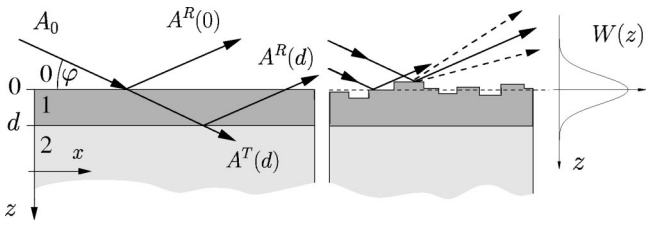

FIG. 1. Left: A wave incident on a thin film is scattered into two channels, corresponding to specular reflection and forward transmission. The layers labeled by 0, 1, and 2 denote vacuum, film, and substrate, respectively. Right: A rough surface introduces relative phases between the scattered waves that result in a reduction of the specularly reflected intensity and scattering into diffuse directions. $W(z)$ is the distribution function of the surface elements along z for the rough surface.

arrives at a set of coupled linear differential equations with constant coefficients. The amplitude in depth z of a homogeneous layer is then given by

$$\mathbf{A}(z) = e^{i\mathbf{F}z}\mathbf{A}(0), \tag{1}$$

where the matrix elements of the propagation matrix $\mathbf{F}$ are the transition amplitudes for scattering processes between the open scattering channels. In the general case, $\mathbf{A} = (\mathbf{A}_1, \mathbf{A}_2, \ldots, \mathbf{A}_n)$ is a multidimensional vector representing the set of field amplitudes in the n open scattering channels. The number of possible scattering channels is determined by the structure of the sample and the scattering geometry.[40] In crystalline samples, e.g., several Bragg and Laue reflections are possible, which are excited if the momentum transfer coincides with a reciprocal-lattice vector. The virtue of this formalism is that it allows one to treat a variety of scattering problems extending from simple forward scattering to diffraction from laterally structured samples.[40] Systems consisting of multiple layers are treated by subsequent multiplication of matrix exponentials. Grazing-incidence reflection is a two-beam case of x-ray diffraction, the (000) Bragg reflection. Thus, one has to consider two scattering channels, i.e., specular reflection R and forward transmission T, as shown in Fig. 1. The propagation matrix of layer i in this case reads[40]

$$\mathbf{F}_i = \begin{pmatrix} \mathbf{f}_i + \mathbf{k}_{0z} & \mathbf{f}_i \\ -\mathbf{f}_i & -\mathbf{f}_i - \mathbf{k}_{0z} \end{pmatrix}, \tag{2}$$

with

$$\mathbf{f}_i = \frac{2\pi}{k_{0z}} \sum_j \rho_j \mathbf{M}_j(\omega) \tag{3}$$

being the scattering matrix for grazing-incidence reflection.[41] The sum runs over all atomic species in the layer with number densities ρ_j each and the energy-dependent forward-scattering length $\mathbf{M}_j(\omega)$ which is a 2×2 matrix to account for the polarization dependence of the scattering process, as explained in the following section. $\mathbf{k}_{0z} = k_{0z}\mathbf{1}$, where k_{0z} is the z component of the wave vector and $\mathbf{1}$ is the 2×2 unit matrix. The solution of the scattering problem becomes comparatively easy in the system of eigenpolarizations of the

sample. Those are the polarization states that remain unchanged in the scattering process. They are obtained by diagonalization of the forward-scattering matrix $\mathbf{f}_i$,

$$\mathbf{f}_{i,D}(\omega)=\mathbf{g}\mathbf{f}_i(\omega)\mathbf{g}^{-1} \quad \text{with} \quad [\mathbf{f}_D(\omega)]_{\mu\nu}=\delta_{\mu\nu}f_{i,\mu}(\omega), \tag{4}$$

with the diagonalizing matrix $\mathbf{g}$ and the eigenvalues $f_{i,\mu}(\omega)$ of the matrix $\mathbf{f}_i$. The matrix exponential can then be calculated for each eigenpolarization separately. Thus, for better readability, we drop the polarization index μ in the following paragraph.

In case of a single layer of thickness d on a semi-infinite substrate, Eq. (1) can be written as[40,42]

$$\begin{pmatrix} A^T(d) \\ A^R(d) \end{pmatrix}=\mathbf{s}(d)\begin{pmatrix} A^T(0) \\ A^R(0) \end{pmatrix}, \tag{5}$$

with

$$\mathbf{s}(d)=\frac{1}{t_{21}}\begin{pmatrix} 1 & r_{21} \\ r_{21} & 1 \end{pmatrix}\begin{pmatrix} e^{ik_{1z}d} & 0 \\ 0 & e^{-ik_{1z}d} \end{pmatrix}\begin{pmatrix} 1 & r_{10} \\ r_{10} & 1 \end{pmatrix}\frac{1}{t_{10}}. \tag{6}$$

Here, the subscripts 0, 1, and 2 denote vacuum, film, and substrate, respectively. k_{1z} is the z component of the wave vector in the film, which is through Snell's law related to the z component k_{0z} of the incident wave vector by

$$k_{1z}=k_{0z}\beta_1 \quad \text{with} \quad \beta_1(\omega)=\sqrt{1+\frac{2f_1(\omega)}{k_{0z}}}. \tag{7}$$

In grazing-incidence geometry, it is a good approximation to write $k_{0z}\approx k_0\varphi$, with φ being the angle of incidence, see Fig. 1. $r_{ij}(\varphi)$ and $t_{ij}(\varphi)$ are the Fresnel reflection and transmission coefficients of the boundary between two media i and j, respectively,

$$r_{ij}=\frac{\beta_i-\beta_j}{\beta_i+\beta_j}, \quad t_{ij}=\frac{2\beta_i}{\beta_i+\beta_j}. \tag{8}$$

To solve Eq. (5) for the specularly reflected field $A^R(0)$, one has to take the boundary conditions into account which are given here by $A^R(d)=0$ and $A^T(0)=A_0$, where A_0 is the amplitude of the incident field. This leads to the reflectivity r_{012} of the layer system being expressed by the elements $[\mathbf{s}]_{21}$ and $[\mathbf{s}]_{22}$ of the matrix $\mathbf{s}(d)$:

$$A^R(0)=r_{012}A_0 \text{ with } r_{012}=-\frac{[\mathbf{s}]_{21}}{[\mathbf{s}]_{22}}. \tag{9}$$

Evaluation of this equation yields the well-known expression for multibeam interference at a thin film, in the field of x-ray physics often referred to as Parratt formula[43]

$$r_{012}=\frac{r_{01}+r_{12}e^{i2k_{1z}d}}{1+r_{01}r_{12}e^{i2k_{1z}d}}. \tag{10}$$

In the kinematical approximation ($k_{1z}d\ll 1$), we can write $e^{ik_{1z}d}\approx 1+ik_{1z}d$ in Eq. (6). Evaluation of Eq. (9) then leads, after some algebra,[44] to the following result for the reflectivity:

$$r_{012}(\omega)=r_{02}(1+if_1(\omega)|t_{02}|^2d)\approx r_{02}e^{if_1(\omega)|t_{02}|^2d}. \tag{11}$$

This is an expression very similar to the description of nuclear forward scattering,[45,46] where the scattered field is given by $A(\omega)=A_0e^{if(\omega)d}$. Since $f_1(\omega)=(k_0/k_{0z})f(\omega)$ (see Ref. 41), the reflection from an ultrathin film can be treated like forward scattering with an "effective" thickness of $d'=d|t_{02}|^2/\varphi$. This value results from two effects. First, d is enhanced by a factor of $1/\sin\varphi\approx 1/\varphi$, which is simply the path length of the radiation traveling under an angle φ through a film of thickness d. Second, an additional thickness enhancement results from x-ray interference effects.[47] $|t_{02}|^2$ is the relative intensity of the standing wave with amplitude A_S that results from the superposition of incident and reflected wave, i.e., $A_S=(1+r_{02})A_0=t_{02}A_0$. This enhanced interaction with the radiation field thus mimics an increased film thickness.

Once the reflectivities for each eigenpolarization have been calculated, the (2×2) reflectivity matrix $\mathbf{R}$ in the original polarization basis is then obtained via the backtransformation

$$\mathbf{R}=\mathbf{g}^{-1}\mathbf{R}_D\mathbf{g} \text{ with } [\mathbf{R}_D]_{\mu\nu}=\delta_{\mu\nu}r_{012,\mu}, \tag{12}$$

where the $r_{012,\mu}$ are the reflectivities for both eigenpolarizations, given by Eq. (11).

So far we have assumed that the boundaries of the layer system were perfectly smooth. This, however, is typically not true for real samples. Figure 1 shows a model of a thin film on a substrate that exhibits a steplike corrugation. Due to the spatial displacement of the surface elements, the amplitude scattered from each of them contributes to the total scattered amplitude with a spatial phase factor. Coherent summation over all these contributions yields for the reflected amplitude

$$r'_{012}=r_{012}\int W(z)\exp\{2ik_{0z}z\}dz, \tag{13}$$

where the distribution function $W(z)$ describes the probability to find an element of the surface in depth z. If $W(z)$ is a Gaussian with standard deviation σ, the integral in Eq. (13) can be calculated exactly and we obtain for the reflected amplitude

$$r'_{012}=r_{012}\exp\{-4k_0^2\varphi^2\sigma^2\}. \tag{14}$$

Thus, the presence of surface roughness introduces a damping factor that is the Fourier transform of the height distribution function $W(z)$. For example, the intensity $|r'_{012}|^2$ of 14.4-keV radiation ($k_0=7.3$ Å^{-1}) that is reflected at $\varphi=5$ mrad from a surface with a roughness of $\sigma=2$ nm, is reduced by a factor of 100 compared to a smooth surface.

The above treatment is valid only if the lateral dimension of the surface elements is smaller than the in-plane transverse coherence length $L_t=L/\varphi$ of the radiation. L is the width of the mutual coherence function that is introduced to describe the degree of coherence of the radiation field.[48] It determines to what degree waves scattered from different parts of the sample have to be added coherently. This plays an important role in the interpretation of x-ray scattering experiments with synchrotron radiation.[48] Due to the small

source size of undulator synchrotron sources, for example, the transverse coherence length at the sample position can be several micrometers.[49] In grazing-incidence geometry, these values increase to L/φ along the x direction (see Fig. 1), so that coherent illumination may occur over in-plane distances of several hundred micrometers. These considerations, however, apply only for the specularly reflected beam. If the detector aperture integrates over an increasing part of the diffusely scattered (off-specular) radiation, the apparent coherence length decreases.[50] As a result, contributions from laterally separated parts of the surface have to be added with a decreasing degree of coherence.

B. The forward-scattering amplitude

The formalism developed above applies for polarization-dependent scattering of hard x rays in grazing-incidence geometry. Polarization mixing effects are typically very pronounced in resonant scattering processes. The functional form and the energy dependence of the scattering process is described by the forward-scattering length

$$\mathbf{M}(\omega)=\mathbf{E}(\omega)+\mathbf{N}(\omega), \tag{15}$$

which consists of two contributions: $\mathbf{E}(\omega)$ describes nonresonant electronic charge scattering (assuming ω being far away from absorption edges) and is given by

$$[\mathbf{E}(\omega)]_{\mu\nu}=(\hat{\boldsymbol{\epsilon}}_\mu\cdot\hat{\boldsymbol{\epsilon}}_\nu)\left[-Zr_0+i\frac{k_0}{4\pi}\sigma_t(\omega)\right], \tag{16}$$

where Z is the atomic number, r_0 is the classical electron radius, and σ_t is the total absorption cross section. $\mathbf{N}(\omega)$ contains the contributions from resonant scattering processes such as resonant magnetic x-ray scattering[11,51] or nuclear resonant scattering.[52–54] For an electric 2^L-pole resonance this scattering length is given by[51]

$$[\mathbf{N}(\omega)]_{\mu\nu}=\frac{4\pi f_R}{k_0}\sum_{M=-L}^{L}[\hat{\boldsymbol{\epsilon}}_\nu\cdot\hat{Y}_{LM}(\hat{k}_0)]\times[\hat{Y}^*_{LM}(\hat{k}_0)\cdot\hat{\boldsymbol{\epsilon}}_\mu]F_{LM}(\omega). \tag{17}$$

The two dot products between the polarization basis vectors $(\hat{\boldsymbol{\epsilon}}_\nu,\hat{\boldsymbol{\epsilon}}_\mu)$ and the vector spherical harmonics $\hat{Y}_{LM}(\hat{k}_0)$ describe the anisotropy of photon absorption and reemission, respectively. The energy dependence of the scattering process is contained in the functions $F_{LM}(\omega)$ as will be explained below. $f_R<1$ describes the degree of elasticity of the scattering process.[55] It is convenient to expand Eq. (17) in powers of the unit vector $\hat{m}$ that defines the magnetic quantization axis of the atom in the sample. The resonant scattering length for an electric dipole transition ($L=1$) can then be written as[53]

$$[\mathbf{N}(\omega)]_{\mu\nu}=\frac{3}{16\pi}\{(\hat{\boldsymbol{\epsilon}}_\mu\cdot\hat{\boldsymbol{\epsilon}}_\nu)[F_{+1}+F_{-1}] -i(\hat{\boldsymbol{\epsilon}}_\mu\times\hat{\boldsymbol{\epsilon}}_\nu)\cdot\hat{m}[F_{+1}-F_{-1}] +(\hat{\boldsymbol{\epsilon}}_\mu\cdot\hat{m})(\hat{\boldsymbol{\epsilon}}_\nu\cdot\hat{m})[2F_0-F_{+1}-F_{-1}]\}. \tag{18}$$

For convenience, we have dropped the subscript L. In the following, the focus will be on *nuclear* dipole transitions. The functions $F_M=F_M(\omega)$ are the energy-dependent resonant strengths for transitions with a change of M in the magnetic quantum number:

$$F_M(\omega)=K\sum_{m_i}\frac{C^2(I_g1I_e;m_iM)}{\hbar(\omega-\omega_{m_iM})+i\Gamma_0/2} \tag{19}$$

with

$$K=\frac{2\pi f_{LM}\Gamma_0}{k_0(1+\alpha)(2I_g+1)},$$

where I_g and I_e are the nuclear spins of the ground and excited states, f_{LM} is the Lamb-Mössbauer factor, Γ_0 the natural linewidth of the transition, and α the coefficient of internal conversion. The sum runs over all ground-state levels with magnetic quantum numbers m_i. ω_{m_iM} is the resonance energy of the transition with the quantum numbers m_i and M. This is illustrated for the 14.4-keV resonance of ^{57}Fe in Fig. 3. The $C(I_g1I_e;m_iM)$ are the Clebsch-Gordan coefficients in the notation of Rose[56] that describe the relative strength of the transitions. In case of a magnetic dipole transition, the role of the electric and magnetic fields of the radiation are interchanged. Then one has to transform the polarization vectors in Eq. (18) according to $\hat{\boldsymbol{\epsilon}}\rightarrow\hat{\boldsymbol{\epsilon}}\times\hat{k}_0$, where $\hat{k}_0$ is a unit vector along the photon wave vector. The three terms in Eq. (18) represent different polarization dependencies. The first term is not sensitive to the sample magnetization. Its polarization dependence given by $\hat{\boldsymbol{\epsilon}}_\mu\cdot\hat{\boldsymbol{\epsilon}}_\nu$ is that of nonresonant charge scattering. The second term describes circular dichroism because it depends on the difference between the resonant scattering amplitudes F_{+1} and F_{-1}. Since its polarization dependence is given by $\hat{\boldsymbol{\epsilon}}_\mu\times\hat{\boldsymbol{\epsilon}}_\nu$, it describes orthogonal scattering, e.g., $\hat{\sigma}\rightarrow\hat{\pi}$ and $\hat{\pi}\rightarrow\hat{\sigma}$. The third term that is proportional to $2F_0-F_{+1}-F_{-1}$ describes linear magnetic dichroism. Its polarization dependence allows for all scattering processes within the given polarization basis. The occurrence of optical activity crucially depends on the orientation of $\hat{m}$. In the following, we assume a sample with a uniaxial magnetization and a linear polarization basis, where σ polarization lies in the plane of the storage ring. The orientation of the magnetic moment with respect to the incident wave vector and the linear polarization basis is sketched in Fig. 2. In general, $\mathbf{f}$ is not Hermitian, so that the eigenpolarizations are not orthogonal and depend explicitly on energy through the functions F_{+1},F_{-1}, and F_0. However, there are some important cases where $\mathbf{f}$ is Hermitian and a system of orthogonal eigenpolarizations can be found so that

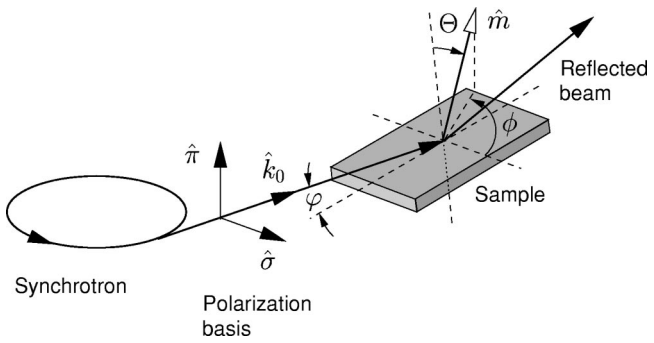

FIG. 2. Relative orientation (Θ,ϕ) of the incident wave vector $\hat{k}_0$ to a unidirectional magnetization $\hat{m}$ of the sample. $(\hat{\sigma},\hat{\pi})$ are the linear polarization basis vectors. The angle of incidence φ is highly exaggerated in this sketch; typical values are a few milli radians.

the diagonalizing matrix **g** in Eq. (4) depends only on the geometry. Those are the cases where the medium possesses global symmetries. This is the case, e.g., for a uniformly magnetized material that exhibits an axial symmetry, so that $\hat{k}_0$ and $\hat{m}$ are parallel or perpendicular to each other. In the latter case, we have $\hat{k}_0 \cdot \hat{m} = 0$, so that

$$\mathbf{f}_D \sim \begin{pmatrix} F_{+1}+F_{-1} & 0 \\ 0 & 2F_0 \end{pmatrix} \text{ and } \mathbf{g} = \begin{pmatrix} \cos\Theta & \sin\Theta \\ -\sin\Theta & \cos\Theta \end{pmatrix}. \tag{20}$$

In this case, the linear polarizations are eigenpolarizations of the system. The diagonalizing matrix describes the rotation of the polarization basis towards the direction of $\hat{m}$. If $\hat{k}_0$ and $\hat{m}$ are parallel, we have the Faraday geometry of magnetic scattering, i.e., $\hat{k}_0 \cdot \hat{m} = 1$, and

$$\mathbf{f}_D \sim \begin{pmatrix} F_{+1} & 0 \\ 0 & F_{-1} \end{pmatrix} \text{ and } \mathbf{g} = \begin{pmatrix} 1 & i \\ i & 1 \end{pmatrix}. \tag{21}$$

Here, the circular polarizations are the eigenpolarizations and the diagonalizing matrix mediates the transformation between the linear and circular polarization basis. Of particular relevance are situations where the directions of magnetic moments are distributed uniformly in space or over certain subspaces that are generated by magnetic anisotropies. In case of thin films, the large magnetic shape anisotropy forces the magnetic moments to be aligned in the plane of the film. In case of unmagnetized multidomain films one often encounters a two-dimensional random distribution of magnetic moments. In these cases, the scattering amplitude can be calculated analytically by integration over the corresponding subspace. The results are summarized in rows E-G of Fig. 5. In these three cases, the scattering matrix $\mathbf{f}(\omega)$ is diagonal in a linear polarization basis.[57]

III. NUCLEAR RESONANT SCATTERING FROM THIN FILMS

So far the formalism was quite general, i.e., no assumptions were made about the type of scattering process that determines the functional shape and the energy dependence

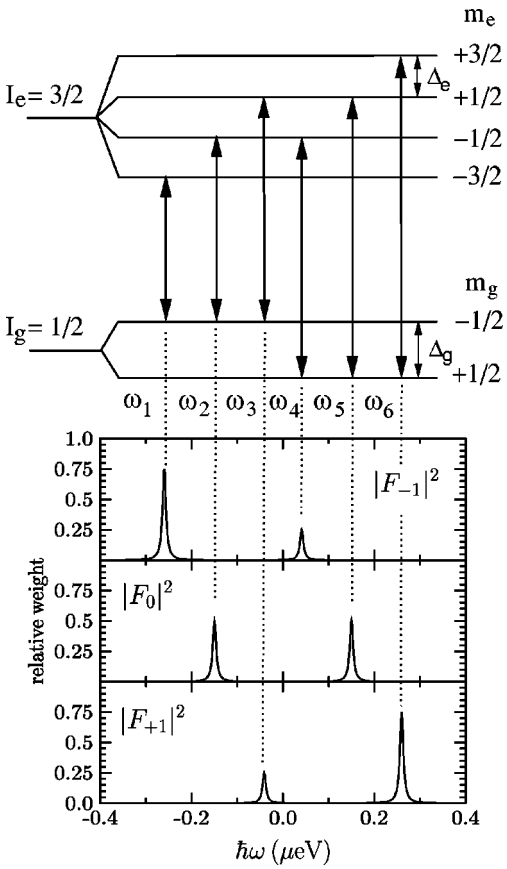

FIG. 3. Nuclear level scheme of the 14.4-keV transition of ^{57}Fe in case of a pure magnetic hyperfine splitting. The six dipole allowed transitions decompose into three different polarization dependencies with their individual energy dependence given by the functions $F_M(\omega)$.

of the functions F_{+1}, F_0, and F_{-1}. This means that the above formalism can be applied to any case of polarization-dependent scattering process that involves electric or magnetic dipole transitions.[58] In the following, we want to discuss the case of nuclear resonant x-ray scattering and demonstrate how this method can be used as a very sensitive probe for thin film and surface magnetism. In particular, we want to concentrate on the 14.4-keV resonance of ^{57}Fe. Due to its large cross section and the large recoil-less fraction this resonance is one of the most widely applied Mössbauer transitions. It is a magnetic dipole transition with spins $I_g = 1/2, I_e = 3/2$ and magnetic moments $\mu_g = 0.091\mu_N, \mu_e = -0.153\mu_N$ of the ground and excited state, respectively, and a natural lifetime of $\tau_0 = 141$ ns. In a magnetic field, the energetic degeneracy of ground and excited states is lifted, resulting in a Zeeman splitting of the nuclear levels, as shown in Fig. 3. Various sources lead to a magnetic field at the position of the nucleus. The main contribution arises from the spin polarization of the *s* electrons via exchange interaction with the spin-polarized *d* electrons. This leads to $B = 33.3$ T in the case of ferromagnetic α-Fe at room temperature, for example. Other contributions arise from dipolar fields, crystal fields, and fields from itinerant electrons. In many cases the total magnetic hyperfine field can be considered proportional to the magnetic moment of the sample.

TABLE I. Parameters of Mössbauer isotopes with resonance energies E_γ below 30 keV that have been used in synchrotron-based experiments. a is the natural abundance of the isotope, I_g and I_e the spins of the ground and excited state, Γ_0 the natural linewidth, and τ the lifetime. σ_0 is the nuclear absorption cross section at resonance. μ_g and μ_e are the magnetic moments of the ground and excited states, given in units of the nuclear magneton μ_N (data partly taken from Ref. 77). The reference in the last column points to the first experiment involving coherent resonant scattering of synchrotron radiation at that resonance.

Isotope	E_γ (keV)	a (%)	Γ_0 (neV)	τ (ns)	σ_0 (10^{-22}m^2)	I_g	I_e	Multi polarity	μ_g (μ_N)	μ_e (μ_N)	Reference
^{181}Ta	6.23	99.9	0.067	9870	1.099	7/2	9/2	$E1$	2.360	5.220	[78]
^{169}Tm	8.41	100	114	5.8	0.242	1/2	3/2	$M1$	−0.232	0.520	[79]
^{83}Kr	9.40	12.0	3.3	212	1.226	9/2	7/2	$M1$	−0.967	−0.939	[80,81]
^{57}Fe	14.41	2.1	4.7	141	2.464	1/2	3/2	$M1$	0.090	−0.155	[82]
^{151}Eu	21.53	47.8	47.0	14.1	0.243	5/2	7/2	$M1$	3.464	2.590	[83]
^{149}Sm	22.49	13.8	64.1	10.3	0.120	7/2	5/2	$M1$	−0.665	−0.622	[84]
^{119}Sn	23.87	8.6	25.7	25.7	1.381	1/2	3/2	$M1$	−1.046	0.685	[85]
^{161}Dy	26.65	18.9	16.2	40.8	1.110	5/2	5/2	$E1$	−0.470	0.558	[86]

However, in the case of ultrathin films the balance between the various contributions may be changed so that the magnetic moment not necessarily follows the evolution of the hyperfine field, as discussed in Ref. 59, for example.

The dipole selection rule $M=m_e-m_g=0,\pm 1$ leads to six allowed transitions, corresponding to six energetically well separated resonances. The resulting energy dependence of the functions $F_M(\omega)$ for $M=-1,0,+1$ is shown in Fig. 3. The energetic positions of the resonance lines are determined by the magnetic hyperfine interaction, i.e.,

$$\hbar\omega_{m_g M}=\hbar\omega_0-(m_e\mu_e-m_g\mu_g)B, \tag{22}$$

where m_e and m_g are the magnetic quantum numbers of the ground and excited state, respectively. $\hbar\omega_0$ is the resonance energy in case of unsplit nuclear levels. After simultaneous excitation of these resonances by a synchrotron-radiation pulse, the time spectrum of the decay exhibits a characteristic quantum beat pattern. The analysis of this pattern enables one to extract information about the magnitude and the directional distribution of hyperfine fields in the sample. In the following, we want to discuss the time-dependent reflectivity of an ultrathin film on a semi-infinite substrate in the general case of polarization-mixing scattering. The substrate is assumed to exhibit no optical activity. After calculation of the energy-dependent reflectivities according to Eq. (11), the time response $\tilde{\mathbf{R}}(t)$ of the system is obtained by Fourier transformation of $\mathbf{R}(\omega)$ as given by Eq. (12):

$$\tilde{\mathbf{R}}(t)=\delta(t)-\tilde{\mathbf{f}}(t)\chi e^{-\chi t/2\tau_0}, \tag{23}$$

with

$$\chi=\frac{1}{4}\rho\sigma_0 f_{\mathrm{LM}}|t_{02}|^2\frac{d}{\varphi}, \tag{24}$$

where $\tilde{\mathbf{f}}(t)$ is the Fourier transform of $\mathbf{f}(\omega)$, ρ is the number density of resonant nuclei, and σ_0 is nuclear absorption cross section at resonance, tabulated for selected isotopes in Table I. The δ function describes the instantaneous radiation pulse that has passed the sample without resonant interaction. The exponential factor $\chi>0$ in Eq. (23) describes the speedup of the decay compared to the natural decay. This is a phenomenon that is characteristic for collective resonant scattering from an ensemble of identical nuclei.[46] For values of about $\chi>3$ the above approximation is not valid anymore, because the time response is then strongly influenced by multiple-scattering events in the sample. This gives rise to an additional beat phenomenon, the so-called dynamical beat or propagation quantum beat,[60,61] that merges with the beat pattern resulting from the hyperfine interaction[62] and complicates the analysis. In the limit of ultrathin films, however, this case is typically not encountered; in the experiments described here, we have observed values of $\chi<1$. A detailed discussion on the limits of the kinematical approximation is given in the Appendix. According to Eq. (23) the maximum delayed intensity is observed at the angle φ, where χ acquires its maximum value. This happens around the critical angle φ_c of the substrate, where $|t_{02}|^2$ assumes its peak value.[63] This is illustrated in Fig. 4, where the time-integrated delayed reflectivity was calculated for 1 ML ^{57}Fe on different substrate materials. At the critical angle the interference between incident and reflected wave forms a standing wave with an antinode exactly at the boundary.

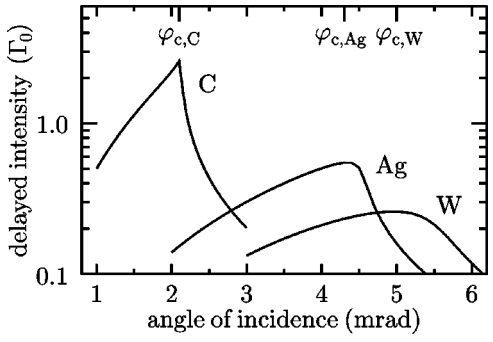

FIG. 4. Time-integrated nuclear resonant reflectivity of a monolayer of ^{57}Fe on various substrates: C, Ag, and W. The intensity peaks at the critical angle φ_c of the substrate, where an antinode of the standing wave coincides with the surface plane.

Since the standing wave slightly penetrates into the substrate, the maximum delayed intensity decreases with increasing photoabsorption of the substrate material. In general, it can be shown that the formation of standing waves above total reflecting surfaces or in x-ray waveguide structures strongly enhances the resonantly scattered signal.[64] The technique thus becomes very sensitive to small amounts of material down to submonolayer coverages.[24]

The information that can be revealed in x-ray scattering from magnetic films critically depends on the polarization state of the incident radiation and the polarization properties of the detector system. Since the polarization of the incident radiation is not necessarily a pure state, we adopt the density-matrix formalism and represent the polarization of the incident beam by a 2×2 matrix $\boldsymbol{\rho}$. The polarization analysis of the scattered photons is described by a polarization filter that is characterized by a 2×2 matrix $\mathbf{P}$. The measured intensity in such a configuration is then given by

$$I=\mathrm{Tr}[\boldsymbol{\rho}\mathbf{R}^{*}\mathbf{P}^{*}\mathbf{P}\mathbf{R}]. \tag{25}$$

The density matrix $\boldsymbol{\rho}$ can be expressed by the three real Stokes' parameters ξ_1,ξ_2, and ξ_3:

$$\boldsymbol{\rho}=\frac{1}{2}\begin{pmatrix}1+\xi_1 & \xi_2-i\xi_3\\ \xi_2+i\xi_3 & 1-\xi_1\end{pmatrix}. \tag{26}$$

The ξ_i assume values between -1 and $+1$ to describe a state within a basis of orthogonal polarizations: ξ_1 refers to a linear polarization basis, ξ_2 to a linear basis rotated by an angle of 45° relative to the previous one, and ξ_3 refers to a circular polarization basis. In the following, we assume an arbitrary degree of linear polarization of the incident beam, i.e., $|\xi_1|\leqslant1$ and $\xi_2=\xi_3=0$. The extreme values of $\xi_1=1$ and $\xi_1=-1$ represent the pure states of σ and π polarization, respectively. Further we assume no polarization analysis of the scattered beam, i.e., $[\mathbf{P}]_{\mu\nu}=\delta_{\mu\nu}$. In this case, one obtains for the scattered intensity

$$I=\frac{1}{2}(1+\xi_1)(|\mathbf{R}_{11}|^2+|\mathbf{R}_{12}|^2)+\frac{1}{2}(1-\xi_1)(|\mathbf{R}_{21}|^2+|\mathbf{R}_{22}|^2), \tag{27}$$

where the $\mathbf{R}_{ij}$ are the matrix elements of $\mathbf{R}$.

Time spectra for some typical magnetization geometries that are often encountered experimentally, are shown in Fig. 5. They were calculated for incident σ polarization and detection without polarization analysis, i.e., $I(t)=|\mathbf{R}_{11}|^2+|\mathbf{R}_{12}|^2$. The sample assumed here was a 2-nm-thick Fe film on W. Obviously, the beat patterns in the spectra characteristically reflect the underlying spin structure. However, there are different spin arrangements that lead to the same time spectrum. Due to this degeneracy, a single time spectrum is not sufficient to determine the spin structure unambiguously. We will show in the following that a reconstruction of the magnetic structure is possible by recording time spectra at a number of sample orientations, e.g., by varying the azimuthal angle ϕ.

IV. EXPERIMENTS

Nanosized particles on surfaces can be produced in a variety of ways. Typical routes are the self-organized growth via condensation out of the gas phase,[65] colloidal agglomeration in solution[66] or the formation on single-crystalline surfaces.[67,68] In this experiment, the latter route was taken to produce single-crystalline island-shaped Fe particles on a W(110) surface. These iron islands were prepared by thermal evaporation of ^{57}Fe (95% enriched) from a crucible under ultrahigh vacuum conditions onto a clean single crystal of W(110). After deposition of Fe, the crystal was heated to about 700 K. At these temperatures, Fe forms separated and well-ordered three-dimensional islands on a pseudomorphically ordered Fe monolayer on W(110).[35] The shape of the islands, depending critically on the thermal treatment, was analyzed by the scanning tunneling microscopy (STM), as shown in Fig. 6. The Fe islands are of bcc(110) type with the lattice constant of bulk iron as revealed by the low-energy electron diffraction (LEED) and x-ray diffraction, as shown in Fig. 7(a). They are of rectangular shape, with the long axis pointing along the W[001] direction. Their average height is 3.7 ± 0.8 nm. Finally, the tungsten crystal was capped with a 2-nm-thick Ag film to prevent oxidation of the Fe islands. The experiments were carried out at the nuclear-resonance beamline ID 18 of the ESRF.[69] Time spectra were partly recorded in the single-bunch filling mode of the storage ring, covering delay times up to 300 ns, and partly taken in the 16-bunch filling mode with the bunches spaced 176 ns apart. The undulator radiation incident on the sample had an energy bandwidth of 6 meV, delivered by a sequence of a heat-load monochromator and a high-resolution monochromator. In a vertical scattering geometry, the sample intercepted a beam cross section of 0.05 mm$\times$2 mm (vertical$\times$horizontal). Maximum countrates were achieved at a grazing angle of 5.2 mrad, close to the critical angle of total reflection of the W substrate. Figure 7(b) shows the angular dependence of the electronic and nuclear reflectivity (upper and lower curve, respectively). The nuclear reflectivity was obtained by integration over a time interval reaching from 20 ns to 300 ns after excitation. Its maximum is observed close to the critical angle of the substrate, consistent with the calculation shown in Fig. 4. Average countrates of up to 40 s^{-1} were observed, allowing a typical data acquisition time per spectrum of about 1 h. We estimate a countrate loss by a factor of 20–30 due to the surface roughness of the W crystal of $\sigma\approx1.2$ nm. Before the measurements the sample was magnetized along the in-plane [001] direction by a pulsed magnetic field of about 50 mT and then kept at remanence in zero external field.

V. RESULTS

A series of time spectra taken at selected azimuthal orientations ϕ of the sample is shown in Fig. 8. Due to the high delayed countrate, the spectra exhibit a good statistical quality up to 300 ns after excitation, covering a dynamic range of more than three orders of magnitude. The beat pattern undergoes characteristic changes that reflect the magnetic spin structure of the islands. With increasing rotation angle ϕ, the

	Geometry	Nuclear Scattering Length $\mathbf{N}(\omega)$	Time spectrum $\sigma \rightarrow$ unpolarized
A	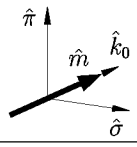	$\frac{3}{16\pi}\begin{pmatrix} F_{+1}+F_{-1} & -\mathrm{i}\,(F_{+1}-F_{-1}) \\ \mathrm{i}\,(F_{+1}-F_{-1}) & F_{+1}+F_{-1} \end{pmatrix}$	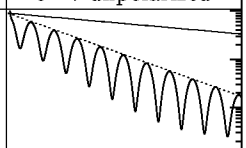
B	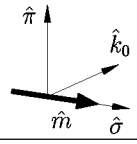	$\frac{3}{16\pi}\begin{pmatrix} F_{+1}+F_{-1} & 0 \\ 0 & 2F_0 \end{pmatrix}$	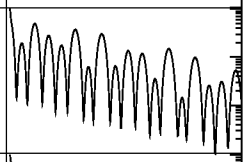
C	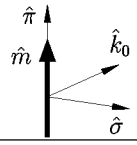	$\frac{3}{16\pi}\begin{pmatrix} 2F_0 & 0 \\ 0 & F_{+1}+F_{-1} \end{pmatrix}$	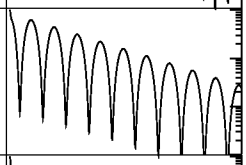
D	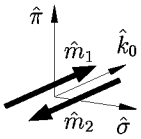	$\frac{3}{16\pi}\begin{pmatrix} F_{+1}+F_{-1} & 0 \\ 0 & F_{+1}+F_{-1} \end{pmatrix}$	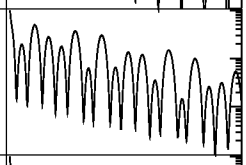
E	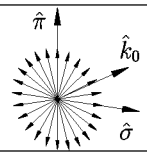	$f_{\sigma\sigma} = f_{\pi\pi} = \frac{3}{32\pi}\,(F_{+1}+F_{-1}+2F_0)$	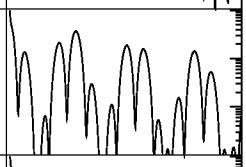
F	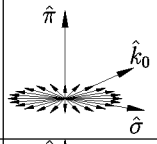	$f_{\sigma\sigma} = \frac{3}{16\pi}\,(F_{+1}+F_{-1})$ $f_{\pi\pi} = \frac{3}{32\pi}\,(F_{+1}+F_{-1}+2F_0)$	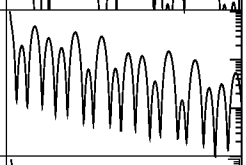
G	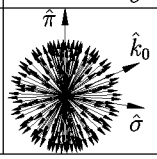	$f_{\sigma\sigma} = f_{\pi\pi} = \frac{1}{8\pi}\,(F_{+1}+F_{-1}+F_0)$	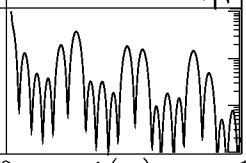
			0 $t\,(\tau_0)$ 1

FIG. 5. Time spectra of nuclear resonant scattering for selected orientations of the magnetic hyperfine field **B**, that defines the direction of the quantization axis $\hat{m}$, relative to the incident wave vector $\hat{k}_0$. The matrix of the nuclear scattering length is given in a linear polarization basis $(\hat{\sigma},\hat{\pi})$. The time spectra are calculated for a 2-nm-thick ^{57}Fe film on a tungsten substrate, assuming purely σ polarized incident radiation and detection without polarization analysis. This is the most frequently used scattering geometry in experiments with synchrotron radiation. A–C display the results for a unidirectional magnetization of the sample. D results from the superposition of two magnetic sublattices in antiparallel alignment. E and F display results for two-dimensional random distributions of spin directions. G shows the result for a three-dimensional random orientational distribution. Since the scattering matrix in the cases E–G is diagonal, only the diagonal elements are shown. The identical shape of the time spectra in rows B, D, and F demonstrates that the spin structure of the sample cannot be determined from just a single time spectrum. Instead, to lift this degeneracy, a number of spectra at different orientations have to be taken. The envelope of the time spectra (dashed line in the upper right figure) indicates that the time response of the film is considerably speeded up compared to the natural decay (solid straight line).

shape and the relative intensities of the individual beats change and new beats appear, resulting from the increasing contribution of higher-frequency components. To deduce hyperfine interaction parameters from the time spectra one has to solve the problem of data inversion. This is, in general, not possible because the phase of the reflected amplitude is lost in the detection process. Nevertheless, some valuable information can already be obtained from a spectral analysis of the measured intensities. A few studies of this kind have been performed in the past,[70–72] but only qualitative results were reported, because the time spectra were influenced by effects of dynamical diffraction. On the other hand, if the scattering process can be treated in the kinematical limit, analytical expressions can be given for the time spectra and their Fourier transforms. This allows one to develop a procedure to reconstruct the magnetic structure of the sample via a Fourier analysis of the measured time spectra, as we will show in the following.

The Fourier transforms of the time spectra are shown in the right panel of Fig. 8. The various spectral components

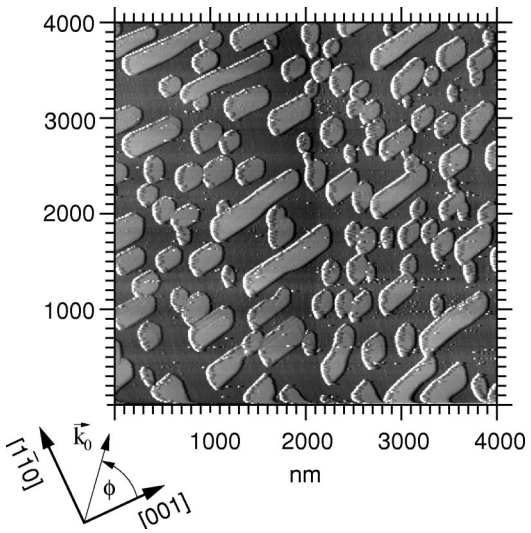

FIG. 6. The STM image of Fe islands on W(110). The islands were produced after deposition of about 5 ML Fe and subsequent annealing for 10 min at 700 K. The elongated islands are aligned along the in-plane [001] direction. In the lower left, the orientation of the photon wave vector relative to the crystallographic axes of the surface is shown. The average height of the islands is 3.7 ± 0.8 nm.

that contribute to the beat pattern show up as peaks with Lorentzian shape. Their energetic positions correspond to those of the $M=\pm 1$ transitions for a magnetic hyperfine field of $B=33.3$ T, as described by Eq. (22). The four frequency differences between these transitions are the beat frequencies that contribute to the time spectrum. This allows already the conclusion that the magnetization of the Fe islands is oriented in the plane of the sample. An additional out-of-plane magnetic moment would lead to extra spectral components at energies different from those observed here.

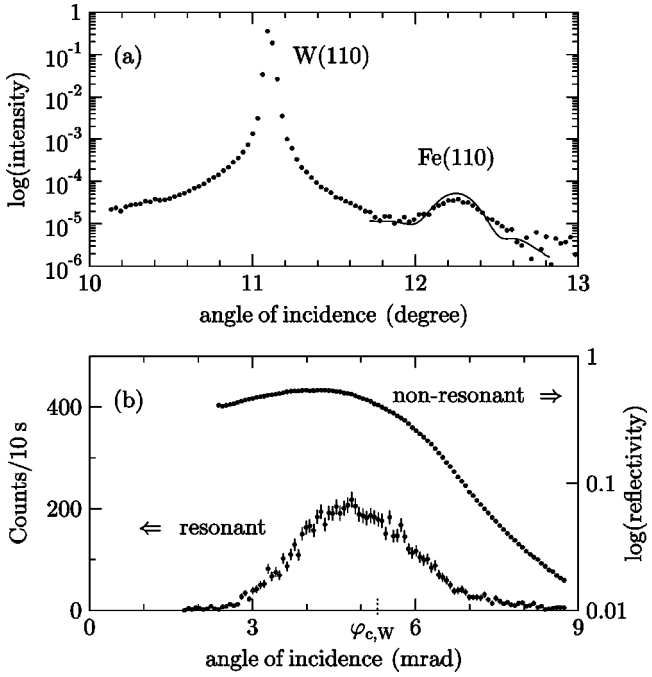

FIG. 7. (a) Reflectivity of the (110) reflection from the W substrate and the Fe islands at 14.4 keV. The solid line is a calculation for the Fe(110) reflection according to the dynamical theory of x-ray diffraction, proving the bcc structure of the Fe islands. (b) Nonresonant reflectivity (upper curve) and resonant reflectivity (lower curve) of the sample. The resonant reflectivity peaks near the critical angle $\varphi_{c,W}$ of the W substrate.

For a quantitative analysis, we chose a linear polarization basis with the σ polarization perpendicular to the scattering plane (see Fig. 2). This corresponds to a Stokes parameter of $\xi_1=1$ ($\xi_1=-1$ if the sample is tilted by 90° for a horizontal scattering plane). Assuming no polarization analysis in the detection process, we obtain for the resonantly reflected intensity according to Eq. (27),

$$I(t)=|\mathbf{R}_{11}|^2+|\mathbf{R}_{12}|^2. \tag{28}$$

Taking only the delayed part of Eq. (23) into account, this equation turns into

$$I(t)=\{|\tilde{\mathbf{f}}_{11}(t)|^2+|\tilde{\mathbf{f}}_{12}(t)|^2\}\chi^2 e^{-\chi t/\tau_0}, \tag{29}$$

$\tilde{\mathbf{f}}(t)$ results from evaluation of Eq. (3) and Fourier transform into the time domain. Since the electronic contribution $\mathbf{E}(\omega)$ to the scattering length is energetically broad, it contributes to the prompt response and need not be considered here. Thus, we evaluate the nuclear contribution $\mathbf{N}(\omega)$ given by Eq. (18) setting $\Theta=\pi/2$, because the magnetization is in the plane of the sample. To account for the general case of several in-plane sublattices, $\mathbf{N}(\omega)$ is the weighted sum over all their contributions. The scattered delayed intensity is then given by

$$I(t)=\{|\tilde{F}_{+1}+\tilde{F}_{-1}|^2+S^2(\phi)|\tilde{F}_{+1}-\tilde{F}_{-1}|^2\}\chi^2 e^{-\chi t/\tau_0}, \tag{30}$$

with

$$S(\phi)=\hat{k}_0\cdot[\mathbf{D}(\phi)\mathbf{M}], \tag{31}$$

$\tilde{F}_M=\tilde{F}_M(t)$ is the Fourier transform of $F_M(\omega)$ that is given in Eq. (19). $\mathbf{M}$ is the magnetic structure function of the sample,

$$\mathbf{M}=\sum_j p_j\hat{m}_j e^{i\mathbf{q}\cdot\mathbf{R}_j} \text{ with } \sum_i p_i=1, \tag{32}$$

where the sum runs over all magnetic sublattices, represented by unit vectors $\hat{m}_j$ and the phase factor accounts for the position $\mathbf{R}_j$ of the atoms. $\mathbf{q}=\mathbf{k}-\mathbf{k}'$ is the momentum transfer in the scattering process. The rotation matrix

$$\mathbf{D}(\phi)=\begin{pmatrix}\cos\phi & \sin\phi\\ -\sin\phi & \cos\phi\end{pmatrix} \tag{33}$$

describes the azimuthal rotation of the sample about the angle ϕ relative to the incident beam. The functions $\tilde{F}_M(t)$ are the superposition of two damped harmonic oscillations given by

$$\tilde{F}_{+1}(t)=(a_1 e^{i\omega_1 t}+a_4 e^{i\omega_4 t})e^{-t/2\tau_0}, \tag{34}$$

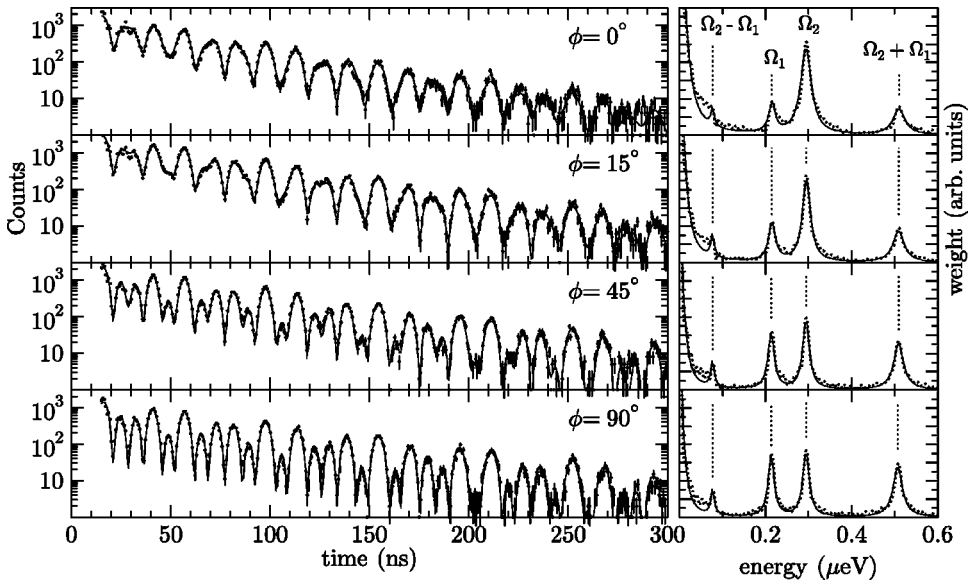

FIG. 8. Time spectra of nuclear resonant scattering from Ag-capped Fe islands on W(110) for various azimuthal orientations in σ geometry. The solid lines are fits according to the theory outlined in the text. The right panel shows the Fourier transform of the measured time spectra to reveal the spectral components that contribute to the beat patttern. The solid lines are Lorentzian fits to the peaks.

$$\tilde{F}_{-1}(t) = (a_3 e^{i\omega_3 t} + a_6 e^{i\omega_6 t}) e^{-t/2\tau_0}. \quad (35)$$

Observing that $a_3 = a_4, a_1 = a_6$ and thus $|\tilde{F}_{+1}(t)|^2 = |\tilde{F}_{-1}(t)|^2$, Eq. (30) can now be written as

$$I(t) = e^{-\chi t/\tau_0}[G(0,0,\Omega_1)\{1 + S^2(\phi)\} + G(\Omega_1 + \Omega_2, \Omega_1 - \Omega_2, \Omega_2)\{1 - S^2(\phi)\}], \quad (36)$$

where the function G is defined as

$$G(c_1, c_2, c_3) = \cos c_1 t + a^2 \cos c_2 t + 2a \cos c_3 t, \quad (37)$$

with $a = a_1/a_4 = a_6/a_3 = 1/3$ being the amplitude ratio of the two resonance lines that comprise $F_M(\omega)$. Ω_1 and Ω_2 are frequency differences between the resonance lines, that can be expressed by the level splittings Δ_g and Δ_e of ground and excited state, respectively (see Fig. 3):

$$\Omega_1 = \omega_4 - \omega_1 = (\Delta_e + \Delta_g)/\hbar, \quad (38)$$

$$\Omega_2 = \omega_3 - \omega_1 = 2\Delta_e/\hbar.$$

Since Eq. (36) is a superposition of damped harmonic functions, its Fourier transform is a superposition of Lorentzians $L(\Omega_i)$ with natural linewidth Γ_0. They are centered around frequencies Ω_i with weight factors $g(\Omega_i)$:

$$I(\omega) = \sum g(\Omega_i) L(\Omega_i) \quad (39)$$

$$= (1 + S^2)(1 + a^2) L(0) + 2a(1 + S^2) L(\Omega_1) + 2a(1 - S^2) L(\Omega_2) + (1 - S^2) L(\Omega_1 + \Omega_2) + a^2 (1 - S^2) L(\Omega_1 - \Omega_2). \quad (40)$$

This means, $S(\phi)$ can be determined from the weights of the Lorentzians $L(\Omega_1)$ and $L(\Omega_2)$ as follows:

$$S = \sqrt{\frac{g(\Omega_1) - g(\Omega_2)}{g(\Omega_1) + g(\Omega_2)}}. \quad (41)$$

In grazing-incidence geometry, the momentum transfer $q \approx k_0 \varphi$ is very small so that the condition $qR \ll 1$ is fulfilled and $e^{i\mathbf{q}\cdot\mathbf{R}_j} \approx 1$ in Eq. (32). Then, with $\hat{k}_0 = (1,0)$ and $\mathbf{M} =: (m_x, m_y)$ the function S is given according to Eq. (31) by

$$S(\phi) = m_x \cos\phi + m_y \sin\phi. \quad (42)$$

In the most simple case of a unidirectional magnetization of the sample with $\mathbf{M} = (1,0)$, and $\hat{k}_0 = (1,0)$ we obtain $S(\phi) = \cos\phi$. This means, the time spectrum $I(t)$ at $\phi = 0$ is a beat pattern with a single frequency Ω_1, as shown in row A of Fig. 5. With ϕ increasing towards $\pi/2$ the modulation becomes more complex due to the admixture of three more frequencies. This corresponds to a rotation of $\hat{m}$ in the $(\hat{\sigma}, \hat{k}_0)$ plane (see Fig. 2), where upon a transition between the time spectra shown in rows A and B of Fig. 5 takes place. However, the measured time spectra for $\phi = 0°$ and $\phi = 90°$ in Fig. 8 slightly deviate from those displayed in rows A and B of Fig. 5. This indicates that the spin structure of the islands cannot be simply unidirectional. To determine the magnetic structure function of the sample, we now apply the algorithm introduced above. The weights $g(\Omega_i)$ are the areas under the Lorentzian functions that were fitted to the spectral components, shown as solid lines in the right panel of Fig. 8. Figure 9(a) shows the weights $g(\Omega_i)$ as a function of azimuthal angle ϕ from which the function $S(\phi)$ was derived according to Eq. (41). The resulting $S(\phi)$ is shown in Fig. 9(b). From a fit of Eq. (42) to the measured function $S(\phi)$ the components m_x and m_y of the magnetic structure function are determined. Here, we obtain the experimental values

$$\mathbf{M}_{exp} = \begin{pmatrix} m_x \\ m_y \end{pmatrix} = \begin{pmatrix} 0.77(3) \\ 0.19(3) \end{pmatrix}. \quad (43)$$

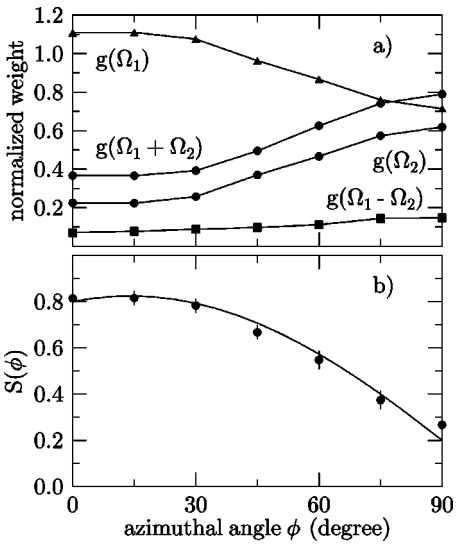

FIG. 9. (a) Dependence of the normalized Fourier components shown in Fig. 8 on the azimuthal angle ϕ. (b) The function $S(\phi)$ as obtained from the data in a) according to Eq. (41). The solid line is a fit of Eq. (42) to the data.

While the determination of $\mathbf{M}_{exp}$ proceeded in an algorithmic and straightforward manner, the determination of the magnetic structure is not that easy: To solve this problem, one has to find a representation of $\mathbf{M}$ as a linear combination of magnetic sublattices $\hat{m}_i$:

$$\begin{pmatrix} m_x \\ m_y \end{pmatrix} = \sum_i p_i \hat{m}_i . \tag{44}$$

that has to fulfill the conditions

$$\sum_i p_i = 1 \quad \text{and} \quad |\hat{m}_i| = 1. \tag{45}$$

From these constraints, it immediately follows that the data cannot be described by a single magnetic sublattice only, because $m_x^2 + m_y^2 \neq 1$. The next step is the assumption of two magnetic sublattices, so that Eq. (44) can be written as

$$\begin{pmatrix} m_x \\ m_y \end{pmatrix} = p_1 \begin{pmatrix} \cos\alpha_1 \\ \sin\alpha_1 \end{pmatrix} + (1-p_1) \begin{pmatrix} \cos\alpha_2 \\ \sin\alpha_2 \end{pmatrix}, \tag{46}$$

where the two angles α_1 and α_2 describe the in-plane orientation of the sublattices relative to the [001] direction. Since this system of equations is underdetermined for the parameters α_1, α_2, and p_1, no unique solution can be given. To discuss the possible solutions of Eq. (46), we rewrite it in form of a matrix equation

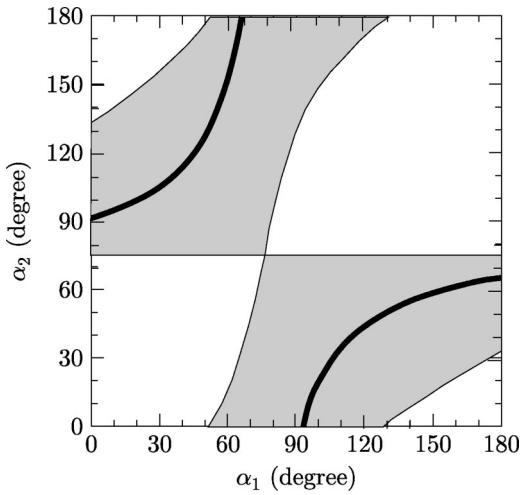

FIG. 10. Graphical representation of the solutions for the angles α_1, α_2 that fulfill the matrix Eq. (47). The shaded area represents angles for which $0 < p_1 < 1$, the solid line fulfills the equation for the second component.

$$\begin{pmatrix} p_1 \\ 1 \end{pmatrix} = \frac{1}{\sin(\alpha_2 - \alpha_1)} \times \begin{pmatrix} \sin\alpha_2 & -\cos\alpha_2 \\ (\sin\alpha_2 - \sin\alpha_1) & (\cos\alpha_1 - \cos\alpha_2) \end{pmatrix} \begin{pmatrix} m_x \\ m_y \end{pmatrix}. \tag{47}$$

The equations for both components have to be fulfilled simultaneously. The manifold of possible solutions is displayed in Fig. 10. While the condition $0 < p_1 < 1$ for the first component is fulfilled for angles α_1 and α_2 in the shaded area, the solid line represents the solutions for the second component. Since this line falls within the shaded area, it represents all solutions of Eq. (46). At this point, the selection of a unique solution has to be guided by additional information about the system. The assumption that one magnetic sublattice is aligned along the long axis of the islands due to the shape anisotropy determines $\alpha_1 = 0°$. It then follows that $\alpha_2 = 90°$ and $p_1 = 0.8$, so that we obtain the following spin structure that lies within the experimental error of the measured values given in Eq. (43):

$$\mathbf{M} = 0.80\hat{u}_{[001]} + 0.20\hat{u}_{[1\bar{1}0]}, \tag{48}$$

where $\hat{u}_{[001]}$ and $\hat{u}_{[1\bar{1}0]}$ are unit vectors along the in-plane [001] and $[1\bar{1}0]$ directions, respectively. Other configurations like closure domains with more than two magnetic sublattices can be excluded here. We can therefore conclude that the Fe islands are laterally separated, single magnetic domains of two different types with their magnetization orthogonal to each other. The algorithm presented here can be applied to determine the magnetic structure of thin films and nanoparticles on surfaces. In many cases, an unambiguous reconstruction can be performed if guided by additional information about the sample. With increasing degree of complexity, however, the reconstruction becomes less unique.

Moreover, it should be noted that the finite temporal range Δt of the measured time spectra limits the energetic resolution of the energy spectra to $\Delta E = h/\Delta t$. This becomes an issue when an additional quadrupole interaction leads to a relative shift of the resonance lines in Fig. 3. The resulting splitting ΔE_Q of the lines at frequencies Ω_1 and Ω_2 in the Fourier spectra can only be resolved if the temporal sampling range is large enough, i.e., $\Delta t > h/\Delta E_Q$, as shown in the case of pure nuclear diffraction from Fe_2O_3.[71]

VI. DISCUSSION

The reconstruction procedure revealed that there are two types of islands, the magnetization of which is aligned in the in-plane [001] direction and $[1\bar{1}0]$ direction, with relative weights of 0.8 and 0.2, respectively. Most probably, this distribution of magnetization directions results from the interplay of different anisotropy energy terms. In this case, we have to consider the contributions of the magnetocrystalline, the magnetoelastic, and the surface anisotropy. However, in the first experimental study of the magnetic anisotropy of closed Fe films on W (110) only the contributions of magnetocrystalline and surface anisotropy had been taken into account.[25] In that case the total free energy F per volume V in the (110) plane depending on the Fe film thickness d has been written as

$$\frac{F}{V} = \frac{K_1}{4}(\sin^2 2\alpha + \sin^4\alpha) - \frac{1}{d}(K_{s,p}^{(1)} + K_{s,p}^{(2)})\sin^2\alpha, \quad (49)$$

with K_1 being the first-order magnetocrystalline anisotropy constant, and $K_{s,p}^{(1)}$ and $K_{s,p}^{(2)}$ describing the surface anisotropies of both interfaces of the film, respectively. Whereas the surface anisotropy, favoring the easy axis along $[1\bar{1}0]$ ($\alpha = \pi/2$), dominates for very small film thicknesses, the magnetocrystalline part forces the magnetization parallel to the in-plane [001] direction ($\alpha = 0$). Both contributions are balanced at around a thickness of 50 ML, where the magnetization rotates from $[1\bar{1}0]$ for thin films to the bulk easy axis [001]. In case of a Ag-capping layer on top of the iron film the surface anisotropy constant is smaller compared to the iron-vacuum interface, leading to the spin reorientation already at around 36 Fe monolayers ($K_{s,p}^{Fe/Ag} = 4.0 \times 10^{-5}$ J/m^2, $K_{s,p}^{Fe/UHV} = 6.5 \times 10^{-5}$ J/m^2).[25] A continuation of this experimental study revealed, however, that due to the quite large Fe-W lattice mismatch of 9.1%, the contribution of the magnetoelastic anisotropy is in the same range as the first-order magnetocrystalline energy and cannot be neglected.[73,74] However, in our case the structural characterization of the islands using x-ray diffraction (see Fig. 7) and LEED shows that the Fe lattice is completely relaxed and strain-free both in horizontal and vertical direction, respectively, leading to the expectation that the magnetoelastic energy is negligible.

In the case of separated islands that exhibit a direction of preferred growth, the in-plane shape anisotropy has additionally to be taken into account. The magnetization along the orientation of the islands ([001]) should energetically be favored, particularly in the islands with high aspect ratios. Since this shape anisotropy is a function of the aspect ratio, it exhibits a statistical distribution. Thus, the distribution of magnetization directions directly reflects the statistics of island shapes and the corresponding contributions of the magnetic shape anisotropy. It turns out, that this contribution is of no relevance in smaller, spherically shaped islands, where the easy magnetization axis points along the $[1\bar{1}0]$ direction as in the case of closed thin iron films on W[110]. In islands with higher aspect ratios the magnetocrystalline and the shape anisotropy, which favor the [001] axis, may together overcome the surface anisotropy. In conclusion, the reorientation of the magnetization from the $[1\bar{1}0]$ to the [001] axis takes place at lower thicknesses than in the closed film due to additional contribution of the pronounced shape anisotropy. This interpretation of shape-dependent reorientation of the magnetization is supported by measurements on another sample with a significantly different size distribution. Islands with already discernable but much less pronounced preferred orientation along the [001] direction have been created by annealing the closed film at lower temperature (600 K), see Fig. 11. Fig. 12 displays a selected set of time spectra for different azimuthal sample orientations. From the Fourier spectra shown in the right panel, we have derived the values $S(\phi)$, as shown in Fig. 14 (squares). The time spectra do not show the pronounced changes with the rotation angle ϕ as the spectra discussed above. While the time spectrum in Fig. 12 at $\phi = 90°$ could be mistaken for that of a unidirectional magnetization as in row B of Fig. 5, only the azimuthal rotation reveals that there must be a significant fraction of a two-dimensional orientational distribution of moments as in row F of Fig. 5. In fact, the spin structure that is extracted from the time spectra is a superposition of two components: One component points along the $[1\bar{1}0]$ direction, i.e., along the direction of the closed iron film, whereas the second part

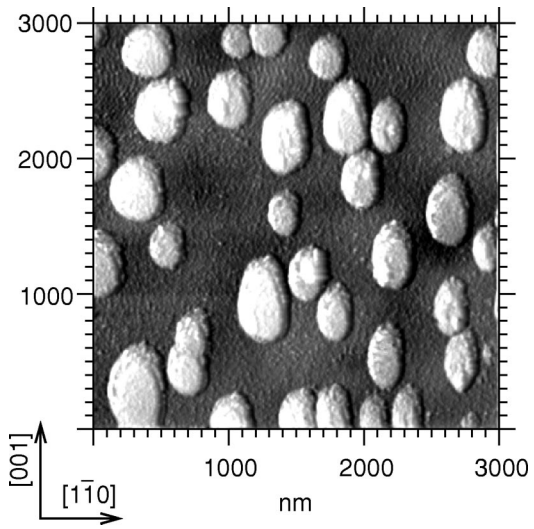

FIG. 11. The STM image of Fe islands on W(110). The islands were produced after deposition of about 5 ML Fe by annealing for 10 min at 600 K. The sample was then capped with Ag. In contrast to Fig. 6, the islands are only slightly elongated along the [001] direction. Their average height is (9.3 ± 1.6) nm.

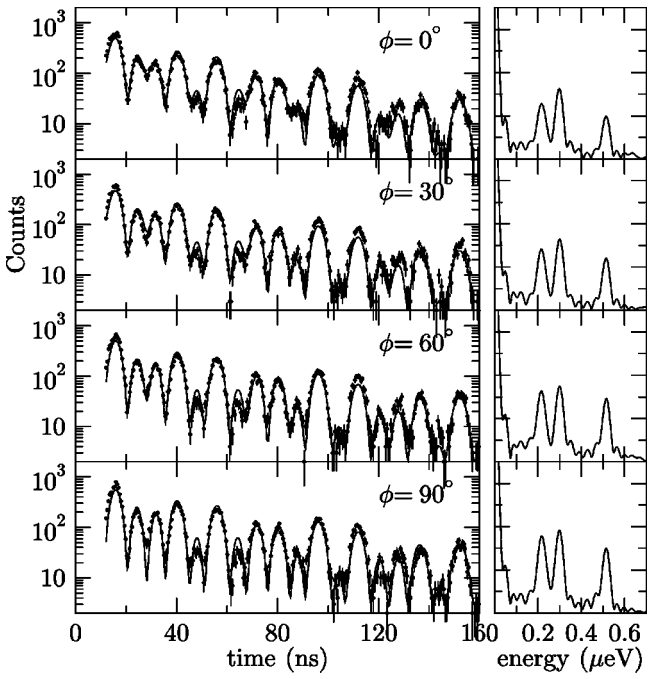

FIG. 12. Time spectra of nuclear resonant scattering from Ag-capped Fe islands on W, as shown in Fig. 11. The time spectra do not show such a pronounced variation with ϕ as those in Fig. 8, pointing to a significant fraction of a two-dimensional random orientation of moments. Accordingly, the Fourier transforms of the time spectra (right panel) look quite alike.

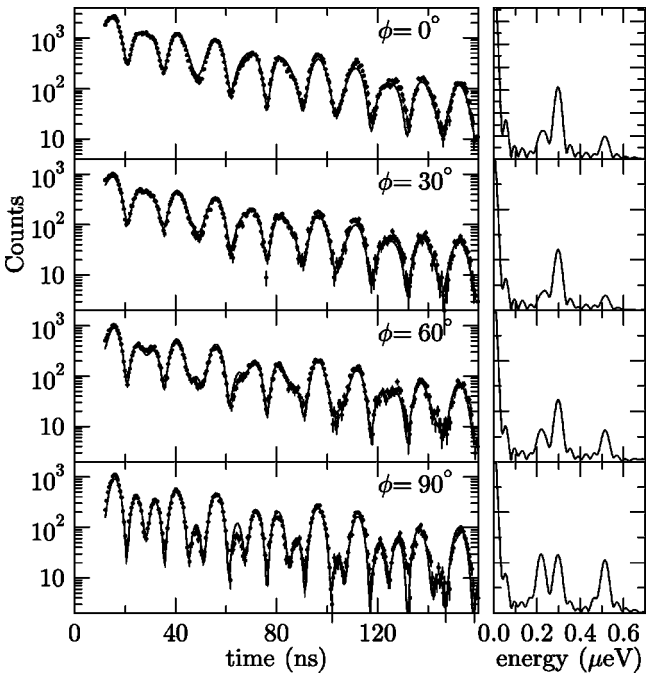

FIG. 13. Time spectra of nuclear resonant scattering from C-capped Fe islands on W for various azimuthal orientations. The angular dependence of these time spectra resembles quite closely that of the spectra in Fig. 8, pointing to the same spin structure.

has to be described by an in-plane random distribution of the magnetization. The relative weights of these components are 60% and 40%, respectively. We can conclude, that the much less distinctive preferred orientation of the islands causes a significant decrease of the total magnetic anisotropy. Here, the contributions of magnetocrystalline and shape anisotropy, on the one hand, and surface anisotropy, on the other hand, are almost balanced. These results are consistent with a vortexlike spin structure in circular Fe islands on W(110) that was reported recently.[75]

In order to study the influence of the capping layer on the magnetic order, we have prepared Fe islands under the same conditions as the sample shown in Fig. 6 (annealing temperature 700 K), and coated them with carbon instead of silver. A set of selected time spectra at various azimuthal positions is shown in Fig. 13. The shape of the time spectra, their Fourier transforms, and the values $S(\phi)$, shown in Fig. 14 (circles), indicate that there is no significant difference compared to those of the Ag-capped islands shown in Fig. 8. The experimental datasets can be simulated assuming the same spin structure as found for the sample discussed above: 80% of the magnetic moments point along the [001] direction, whereas the remaining 20% lie perpendicular along the $[1\bar{1}0]$ axis. Although the capping layer is known to change the surface anisotropy constant in Eq. (49), a difference between Ag and C coverage is not detectable in our experiment. From the comparison of the two capping layers, we have confidence that the rotation of the magnetization really reflects the thickness and shape-dependent interplay of various magnetic anisotropies in the islands—magnetocrystalline, surface and shape—and is not the result of a particular capping layer. The thickness dependence of this interplay was subject of a former study using the x-ray magnetooptical Kerr effect.[76] With increasing thickness of the initially closed Fe film, a spin reorientation of the islands from the $[1\bar{1}0]$ direction into the [001] direction was observed.

It might be worthwhile to note, that although carbon is expected to diffuse into iron, the time spectra do not show any sign of an extra hyperfine component that would hint to a contribution of iron carbide. This is reasonable because C usually diffuses along grain boundaries. Due to the single-crystalline nature of the Fe islands there are no ways for C to penetrate into the Fe lattice. The spin structure of the Fe islands therefore remains unchanged.

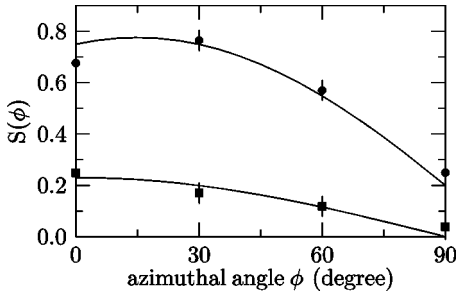

FIG. 14. The function $S(\phi)$ for the Fe islands annealed at 700 K (circles) and annealed at 600 K (squares). The former are capped with C, the latter with Ag. Since the capping has no influence on the spin structure, the differences between the curves is related to the shape of the islands. The solid lines are fits of Eq. (42) to the data.

VII. SUMMARY AND OUTLOOK

The experiments have shown that relaxed Fe islands on W(110) display a multitude of magnetic ordering phenomena, depending on the average thickness and the annealing conditions. The magnetic structure was determined by nuclear resonant scattering of synchrotron radiation. A procedure was developed to extract the magnetic structure function from a series of measurements taken at various azimuthal orientations. Due to the very high brilliance of modern synchrotron-radiation sources, the method is sensitive to coverages down to the submonolayer regime.[24] This opens unique applications in the field of nanoscale magnetism: In combination with other x-ray scattering methods the relation between structural properties and the magnetic behavior of deposited clusters can be explored. Moreover, due to the isotopic selectivity of the scattering process, magnetic properties can be determined with atomic resolution by selectively doping the sample with the Mössbauer nuclei.[64] Another promising application is the determination of internal magnetic fields in oriented biomolecules on surfaces that are considered as future magnetic storage devices.

It seems attractive to extend this technique also to other isotopes with low-energy nuclear transitions. For comparison, the parameters of several Mössbauer isotopes with resonances below 30 keV that have already been used in experiments with synchrotron radiation are listed in Table I. Interesting candidates for magnetic studies are the rare-earth isotopes ^{169}Tm, ^{151}Eu, ^{149}Sm, and ^{161}Dy. Present-day undulators at third generation sources typically deliver a flux of 10^3–10^4 photons/s/neV at photon energies in the range of 10–30 keV. These numbers show that *elastic* nuclear resonant scattering of synchrotron radiation is an attractive technique to study magnetism with monolayer sensitivity. In the same experimental setup it is possible to probe lattice dynamics via *inelastic* nuclear resonant scattering[87,88] that could be shown to exhibit monolayer sensitivity.[89,90] The combination of both techniques offers the unique possibility to study magnetic and vibrational properties and their interrelationship with atomic resolution.

ACKNOWLEDGMENTS

It is a pleasure to thank R. Rüffer for providing excellent experimental conditions at the nuclear-resonance beamline ID18 of the ESRF, for stimulating discussions and for critical reading of the manuscript. Moreover, we wish to acknowledge the support of E. Burkel during the experiments. This work was supported by the German BMBF under contract 05 SK8HR 1 and by the European Union under Contract No. G5RD-CT-2001-00478.

APPENDIX: VALIDITY OF THE KINEMATICAL APPROXIMATION

The procedure for determination of the magnetic structure function as outlined in Sec. V is valid for ultrathin films in the limit of kinematical scattering. With increasing film thickness, however, multiple-scattering processes have to be taken into account. The time spectra are then modulated by a long-period temporal oscillation, the so-called dynamical beat, that imposes restrictions on the applicability of the numerical algorithm described here. Here, we want to quantify the validity limit of this algorithm in terms of film thickness d and number density ρ of resonant nuclei. The first node of the dynamical beat is located at time

$$t_M \approx \frac{16\varphi}{f_{\mathrm{LM}}\sigma_0\rho d}\,\tau_0, \tag{A1}$$

where σ_0 is the nuclear absorption cross section as given in Table I. For times $t<t_M$ the envelope of the time spectra is given by $e^{-(1+\chi)t/\tau_0}$. After multiplication with $e^{\chi t/\tau_0}$ the speedup of the envelope is corrected for and the numerical algorithm can be reliably applied. On the other hand, in the region around $t=t_M$ the time spectra are strongly perturbed. This is illustrated in Fig. 15. Time spectra of grazing-incidence reflection from Fe films on W have been calculated according to the full dynamical theory.[91] It is obvious that with increasing thickness the first node of the dynamical beat, indicated by the shaded region, shifts to earlier times.[92] In the corresponding Fourier spectra, the lines are broadened and their relative intensities are changed so that the spectral weights $g(\Omega_i)$ cannot be determined reliably anymore. According to Eq. (A1) the area density ρd of the resonant nuclei determines the time range Δt that is not perturbed by dynamical beats.[93,94] If one asks for $\Delta t=300$ ns as in our experiments, the critical area density is given by 1.8×10^{20} m^{-2} (assuming that $f_{\mathrm{LM}}=0.8$ and $\varphi=5$ mrad). For pure ^{57}Fe with $\rho=8.46\times10^{28}$ m^{-3} this limit is exceeded

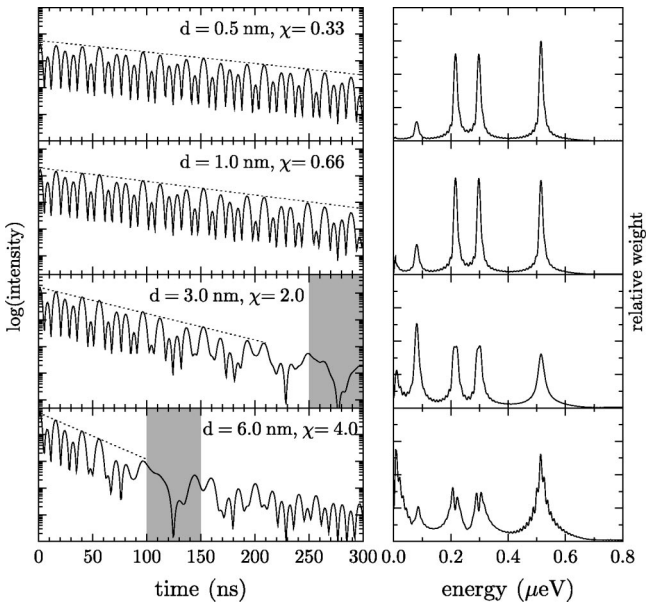

FIG. 15. Time spectra of grazing incidence reflection from ^{57}Fe films on W at $\varphi = 5$ mrad in the magnetization geometry of row B of Fig. 5. The dashed lines mark the envelope that is characterized by the speedup χ. The right panel shows the Fourier spectra of the time spectra in the left panel.

already for $d > 2.2$ nm. If films of larger thicknesses are to be studied by this method, the degree of enrichment should be decreased. On the other hand, one could decrease the time range Δt that is subject to the Fourier transform. This goes, however, at the expense of energetic resolution in the Fourier spectra. Thus, for best results, the speedup should be below $\chi = 1$ and the time spectra should extend over a large temporal range.

[1] *Ultrathin Magnetic Structures*, edited by J.A.C. Bland and B. Heinrich (Springer, Berlin, 1994), Vols. I and II.

[2] J. Magn. Magn. Mater. **200** (1999). special issue on magnetism beyond 2000, edited by A.J. Freeman and S.D. Bader.

[3] S.A. Wolf, D.D. Awschalom, R.A. Buhrmann, J.M. Daughton, S. von Molnár, M.L. Roukes, A.Y. Chtchelkanova, and D.M. Treger, Science (Washington, DC, U.S.) **294**, 1488 (2001).

[4] M.R. Freeman and B.C. Choi, Science (Washington, DC, U.S.) **294**, 1484 (2001).

[5] C.M. Schneider *et al.*, Appl. Phys. Lett. **63**, 2432 (1993); J. Stöhr *et al.*, Science (Washington, DC, U.S.) **259**, 658 (1993).

[6] J. Unguris, G. Hembree, R.J. Celotta, and D.T. Pierce, J. Microsc. **139**, RP1 (1985); H.P. Oepen and J. Kirschner, Scanning Microsc. **5**, 1 (1991).

[7] Y. Martin and H.K. Wickramasinghe, Appl. Phys. Lett. **50**, 1455 (987); J.J. Sáenz *et al.*, J. Appl. Phys. **62**, 4293 (1987).

[8] R. Wiesendanger, H.J. Güntherodt, G. Güntherodt, R.J. Gambino, and R. Ruf, Phys. Rev. Lett. **65**, 247 (1990).

[9] S. Heinze, M. Bode, A. Kubetzka, O. Pietzsch, X. Nie, S. Blügel, and R. Wiesendanger, Science (Washington, DC, U.S.) **288**, 1805 (2000).

[10] J.F. Ankner and G.P. Felcher, J. Magn. Magn. Mater. **200**, 741 (1999).

[11] S.W. Lovesey and S.P. Collins, *X-ray Scattering and Absorption by Magnetic Materials* (Clarendon Press, Oxford, 1996).

[12] Hyperfine Interact. **123/124** (1999); **125** (2000), special issues on nuclear resonant scattering of synchrotron radiation, edited by E. Gerdau and H. de Waard.

[13] S. Bernstein and E.C. Campbell, Phys. Rev. **132**, 1625 (1963).

[14] F. Wagner, Z. Phys. **210**, 361 (1968).

[15] J.C. Frost, B.C.C. Cowie, S.N. Chapman, and J.F. Marshall, Appl. Phys. Lett. **47**, 581 (1985).

[16] R. Röhlsberger, E. Witthoff, E. Gerdau, and E. Lüken, J. Appl. Phys. **74**, 1933 (1993).

[17] S.M. Irkaev, M.A. Andreeva, V.G. Semenov, G.N. Beloserskii, and O.V. Grishin, Nucl. Instrum. Methods Phys. Res. B **74**, 545 (1993); **74**, 554 (1993).

[18] R. Röhlsberger, E. Gerdau, E. Lüken, H.D. Rüter, J. Metge, and O. Leupold, Z. Phys. B: Condens. Matter **92**, 489 (1993).

[19] A.I. Chumakov, G.V. Smirnov, A.Q.R. Baron, J. Arthur, D.E. Brown, S.L. Ruby, G.S. Brown, and N.N. Salashchenko, Phys. Rev. Lett. **71**, 2489 (1993).

[20] T.S. Toellner, W. Sturhahn, R. Röhlsberger, E.E. Alp, C.H. Sowers, and E.E. Fullerton, Phys. Rev. Lett. **74**, 3475 (1995).

[21] D.L. Nagy, L. Bottyán, L. Deák, J. Dekoster, G. Langouche, V.G. Semenov, H. Spiering, and E. Szilágyi, in *Proceedings of Mössbauer Spectroscopy in Materials Science*, edited by M. Miglierini and D. Petridis (Kluwer Academic Press, Amsterdam, 1999), p. 323.

[22] A.I. Chumakov, L. Niesen, D.L. Nagy, and E.E. Alp, Hyperfine Interact. **123/124**, 427 (1999).

[23] L. Niesen, A. Mugarza, M.F. Rosu, R. Coehoorn, R.M. Jungblut, F. Roozeboom, A.Q.R. Baron, A.I. Chumakov, and R. Rüffer, Phys. Rev. B **58**, 8590 (1998).

[24] R. Röhlsberger, J. Bansmann, V. Senz, K.L. Jonas, A. Bettac, O. Leupold, R. Rüffer, E. Burkel, and K.H. Meiwes-Broer, Phys. Rev. Lett. **86**, 5597 (2001).

[25] U. Gradmann, J. Korecki, and G. Waller, Appl. Phys. A: Solids Surf. **39**, 101 (1986).

[26] M. Przybylski and U. Gradmann, Phys. Rev. Lett. **59**, 1152 (1987).

[27] S.C. Hong, A.J. Freeman, and C.L. Fu, Phys. Rev. B **38**, 12 156 (1988).

[28] M. Przybylski, I. Kaufmann, and U. Gradmann, Phys. Rev. B **40**, 8631 (1989).

[29] W. Weber, D. Kerkmann, D. Pescia, D.A. Wesner, and G. Güntherodt, Phys. Rev. Lett. **65**, 2058 (1990).

[30] H.J. Elmers, G. Liu, and U. Gradmann, Phys. Rev. Lett. **63**, 566 (1989).

[31] H.J. Elmers, J. Hauschild, H. Höche, U. Gradmann, H. Bethge, D. Heuer, and U. Köhler, Phys. Rev. Lett. **73**, 898 (1994).

[32] D. Sander, R. Skomski, C. Schmidthals, A. Enders, and J. Kirschner, Phys. Rev. Lett. **77**, 2566 (1996).

[33] N. Weber, K. Wagner, H.J. Elmers, J. Hauschild, and U. Gradmann, Phys. Rev. B **55**, 14 121 (1997).

[34] O. Pietzsch, A. Kubetzka, M. Bode, and R. Wiesendanger, Science (Washington, DC, U.S.) **292**, 2053 (2001).

[35] M. Bode, R. Pascal, and R. Wiesendanger, J. Vac. Sci. Technol. A **15**, 1285 (1997).

[36] L. Lu, J. Bansmann, and K.H. Meiwes-Broer, J. Phys.: Condens. Matter **10**, 2873 (1998).

[37] D. Sander, R. Skomski, A. Enders, C. Schmidthals, D. Reuter, and J. Kirschner, J. Phys. D **31**, 663 (1998).

[38] J. Bansmann, Appl. Phys. A: Mater. Sci. Process. **72**, 447 (2001).

[39] B.W. Batterman and H. Cole, Rev. Mod. Phys. **36**, 681 (1964).

[40] R. Röhlsberger, Hyperfine Interact. **123/124**, 301 (1999).

[41] In case of forward scattering, e.g., transmission through a foil, the propagation matrix is given by $\mathbf{F} = \mathbf{f} + \mathbf{k}_0$ with $\mathbf{f} = (2\pi/k_0)\Sigma_j \rho_j \mathbf{M}_j(\omega)$. The field amplitude in depth z is then, as expected, given by $A(z) = A(0)e^{i\mathbf{n}k_0 z}$ with $\mathbf{n} = 1 + \mathbf{f}/k_0$ being the index of refraction of the material.

[42] L. Deák, L. Bottyán, D.L. Nagy, and H. Spiering, Phys. Rev. B **53**, 6158 (1996).

[43] L.G. Parratt, Phys. Rev. **95**, 359 (1954).

[44] In the derivation, we have made use of the relation $r_{02} = (r_{01} + r_{12})/(1 + r_{01}r_{12})$. Moreover, we have assumed that the angle of incidence φ is below the critical angle of the substrate. In that case, the quantity β_2 is almost purely imaginary so that $4/(1 - \beta_2^2) \approx 4/|1 + \beta_2|^2 = |t_{02}|^2$.

[45] J.B. Hastings, D.P. Siddons, U. van Bürck, R. Hollatz, and U. Bergmann, Phys. Rev. Lett. **66**, 770 (1991).

[46] U. van Bürck, D.P. Siddons, J.B. Hastings, U. Bergmann, and R.

Hollatz, Phys. Rev. B **46**, 6207 (1992).
[47] Similar considerations were performed in Ref. 93 with the result of $|t_{01}|^2$ in Eq. (11) being replaced by t_{01}^2. This approximation, however, is valid only for very low coverages in the monolayer regime.
[48] S.K. Sinha, M. Tolan, and A. Gibaud, Phys. Rev. B **57**, 2740 (1998).
[49] E. Gluskin, E.E. Alp, I. McNulty, W. Sturhahn, and J. Sutter, J. Synchrotron Radiat. **6**, 1065 (1999).
[50] A.Q.R. Baron, A.I. Chumakov, H.F. Grünsteudel, H. Grünsteudel, L. Niesen, and R. Rüffer, Phys. Rev. Lett. **77**, 4808 (1996).
[51] J.P. Hannon, G.T. Trammell, M. Blume, and D. Gibbs, Phys. Rev. Lett. **61**, 1245 (1988).
[52] J.P. Hannon and G.T. Trammell, Phys. Rev. **169**, 315 (1968); **186**, 306 (1969).
[53] J.P. Hannon and G.T. Trammell, Hyperfine Interact. **123/124**, 127 (1999).
[54] W. Sturhahn and E. Gerdau, Phys. Rev. B **49**, 9285 (1994).
[55] In the case of inner-shell resonances where the scattering proceeds on a time scale of $\approx 10^{-16}$ s, f_R equals the Debye-Waller factor f_D, in the case of nuclear resonances with lifetimes of up to several microseconds, f_R is the Lamb-Mössbauer factor f_{LM}.
[56] M.E. Rose, *Elementary Theory of Angular Momentum* (Wiley, New York, 1957).
[57] R. Röhlsberger, O. Leupold, J. Metge, H.D. Rüter, W. Sturhahn, and E. Gerdau, Hyperfine Interact. **92**, 1107 (1994).
[58] A. Rühm, B.P. Toperverg, and H. Dosch, Phys. Rev. B **60**, 16073 (1999).
[59] M. Przybylski, Hyperfine Interact. **113**, 135 (1998).
[60] D. Fröhlich, A. Kulik, B. Uebbing, A. Mysyrowicz, V. Langer, H. Stolz, and W. von der Osten, Phys. Rev. Lett. **67**, 2343 (1991).
[61] U. van Bürck, W. Potzel, P. Schindelmann, Yu.V. Shvyd'ko, E. Gerdau, O. Leupold, and H.D. Rüter, Phys. Rev. A **61**, 013803 (2000).
[62] Yu.V. Shvyd'ko, U. van Bürck, W. Potzel, P. Schindelmann, E. Gerdau, O. Leupold, J. Metge, H.D. Rüter, and G.V. Smirnov, Phys. Rev. B **57**, 3552 (1998).
[63] A.Q.R. Baron, J. Arthur, S.L. Ruby, A.I. Chumakov, G.V. Smirnov, and G.S. Brown, Phys. Rev. B **50**, 10 354 (1994).
[64] R. Röhlsberger, H. Thomas, K. Schlage, E. Burkel, O. Leupold, and R. Rüffer, Phys. Rev. Lett. **89**, 237201 (2002).
[65] R.H. Kodama and A.S. Edelstein, J. Appl. Phys. **85**, 4316 (1999).
[66] S. Sun, C.B. Murray, D. Weller, L. Folks, and A. Moser, Science (Washington, DC, U.S.) **287**, 1989 (2000).
[67] *Metal Clusters at Surfaces*, edited by K. H. Meiwes-Broer (Springer, Berlin, 2000).
[68] S. Padovani, J. Chado, F. Scheurer, and J.P. Bucher, Phys. Rev. B **59**, 11 887 (1999).
[69] R. Rüffer and A.I. Chumakov, Hyperfine Interact. **97/98**, 589 (1996), see also http://www.esrf.fr/exp_facilities/ID18/
[70] J.R. Grover, D.P. Siddons, J.B. Hastings, G. Faigel, L.E. Berman, and P.E. Haustein, Hyperfine Interact. **62**, 35 (1990).
[71] S. Kikuta, in *Proceedings of the International Conference on Anomalous Scattering*, Malente, Germany, 1992, edited by G. Materlik, C.J. Sparks, and K. Fischer (Elsevier, Amsterdam, 1994).
[72] M.A. Andreeva, V.G. Semenov, L. Häggström, B. Lindgren, B. Kalska, A.I. Chumakov, O. Leupold, R. Rüffer, K.A. Prokhorov, and N.N. Salashchenko, Phys. Met. Metallogr. **91**, 22 (2001).
[73] H.J. Elmers and U. Gradmann, Appl. Phys. A: Solids Surf. **51**, 255 (1990).
[74] P. Baumgart, B. Hillebrands, and G. Güntherodt, J. Magn. Magn. Mater. **93**, 225 (1991).
[75] A. Wachowiak, J. Wiebe, M. Bode, O. Pietzsch, M. Morgenstern, and R. Wiesendanger, Science (Washington, DC, U.S.) **298**, 577 (2002).
[76] V. Senz, A. Kleibert, and J. Bansmann, Surf. Rev. Lett. **9**, 913 (2002).
[77] J.G. Stevens and V.E. Stevens, *Mössbauer Effect Data Index* (Plenum Press, New York, 1973).
[78] A.I. Chumakov, A.Q.R. Baron, J. Arthur, S.L. Ruby, G.S. Brown, G.V. Smirnov, U. van Bürck, and G. Wortmann, Phys. Rev. Lett. **75**, 549 (1995).
[79] W. Sturhahn, E. Gerdau, R. Hollatz, R. Rüffer, H.D. Rüter, and W. Tolksdorf, Europhys. Lett. **17**, 821 (1991).
[80] A.Q.R. Baron, A.I. Chumakov, S.L. Ruby, J. Arthur, G.S. Brown, G.V. Smirnov, and U. van Bürck, Phys. Rev. B **51**, 16 384 (1995).
[81] D.E. Johnson, D.P. Siddons, J.Z. Larese, and J.B. Hastings, Phys. Rev. B **51**, 7909 (1995).
[82] E. Gerdau, R. Rüffer, H. Winkler, W. Tolksdorf, C.P. Klages, and J.P. Hannon, Phys. Rev. Lett. **54**, 835 (1985).
[83] O. Leupold, J. Pollmann, E. Gerdau, H.D. Rüter, G. Faigel, M. Tegze, G. Bortel, R. Rüffer, A.I. Chumakov, and A.Q.R. Baron, Europhys. Lett. **35**, 671 (1996).
[84] R. Röhlsberger, K.W. Quast, T.S. Toellner, P.L. Lee, W. Sturhahn, E.E. Alp, and E. Burkel, Phys. Rev. Lett. **87**, 047601 (2001).
[85] E.E. Alp, T.M. Mooney, T. Toellner, W. Sturhahn, E. Witthoff, R. Röhlsberger, E. Gerdau, H. Homma, and M. Kentjana, Phys. Rev. Lett. **70**, 3351 (1993).
[86] Yu.V. Shvyd'ko, M. Gerken, H. Franz, M. Lucht, and E. Gerdau, Europhys. Lett. **56**, 309 (2001).
[87] M. Seto, Y. Yoda, S. Kikuta, X.W. Zhang, and M. Ando, Phys. Rev. Lett. **74**, 3828 (1995).
[88] W. Sturhahn, T.S. Toellner, E.E. Alp, X. Zhang, M. Ando, Y. Yoda, S. Kikuta, M. Seto, C.W. Kimball, and B. Dabrowski, Phys. Rev. Lett. **74**, 3832 (1995).
[89] R. Röhlsberger, W. Sturhahn, T.S. Toellner, K.W. Quast, E.E. Alp, A. Bernhard, J. Metge, R. Rüffer, and E. Burkel, Physica B **263-264**, 581 (1999).
[90] W. Sturhahn, R. Röhlsberger, E.E. Alp, T. Ruckert, H. Schrör, and W. Keune, J. Magn. Magn. Mater. **198-199**, 590 (1999).
[91] The dynamical theory of nuclear resonant scattering was implemented in the program package CONUSS that is described in detail in Refs. 54 and 94. It was extended to grazing-incidence reflection from thin films, as explained in Ref. 40.
[92] In case of a magnetic hyperfine interaction, the dynamical beats contain contributions from hyperfine transitions of different strength. For a detailed investigation see Ref. 62, in particular, Fig. 4(a) therein.
[93] M.A. Andreeva and B. Lindgren, Pis'ma Zh. Eksp. Teor. Fiz. **76**, 833 (2002).
[94] W. Sturhahn, Hyperfine Interact. **125**, 149 (2000).